

# A SCALABLE WALL FUNCTION APPROACH FOR HIGH REYNOLDS NUMBER FLOWS

*P. Catalano, P.L. Vitagliano*

CIRA – Italian Aerospace Research Center, Italy

The simulation of wall-bounded flows requires an appropriate mesh in order to capture the large gradients occurring close to solid boundaries. The near-wall grid requirements become more and more severe increasing the Reynolds number. This paper presents a wall boundary conditions formulation that allows to relax the grid-resolution requirements within the RANS methodology. The issue of the location of first integration point, and of the singularity close to separation and re-attachment points is discussed.

## Introduction

A scalable wall function approach has been developed by the authors in the framework of the E.C. funded project EUROLIFT II (contract no. AST2-2004-502896). The adopted formulation follows the near-wall treatment of the Navier-Stokes equations as proposed by Grotjans and Menter [1] and has been applied to simulate two-dimensional and three-dimensional flows at transonic and high lift conditions. For the transonic flow around

the RAE 2822 airfoil, and for the high lift flow around a three-component airfoil in landing configuration, computational meshes with different sizes of the wall-adjacent cells have been employed. The wing-body KH3Y in high lift conditions has also been considered. This configuration was tested during the EUROLIFT I project [2] (contract no. G4RD-CT-1999-00072) at a Reynolds number of about  $1.3 \times 10^6$  in the low speed wind tunnel LSWT of Airbus-D in Bremen, and at Reynolds numbers up to  $1.5 \times 10^7$  in the European Transonic Wind tunnel ETW in Cologne. The wall function approach has been applied to perform simulations around the KHY3 geometry at the higher Reynolds number employing the same mesh used for the lower Reynolds number case.

## Formulation

In the cells close to an adiabatic wall, the evaluation of the momentum diffusive fluxes (i.e. stress tensor) requires the computation of the velocity gradients. A fine mesh would be necessary in order to properly evaluate the ve-

locity derivatives. The wall functions allow to obtain the stress tensor at the wall without the computation of the velocity gradient components.

*Determination of the wall stress components.*

Let us consider a global Cartesian reference system  $(x_1, x_2, x_3)$ , and a local reference system  $(\xi_1, \xi_2, \xi_3)$  with the  $\xi_2$  axis in the wall-normal direction. The derivatives of the velocity in the stream and span wise directions are zero at the wall for the no-slip condition, and the stress tensor can be written as :

$$\tau_{ij}|_w = \mu \left[ \frac{\partial u_i}{\partial \xi_2} \frac{\partial \xi_2}{\partial x_j} + \frac{\partial u_j}{\partial \xi_2} \frac{\partial \xi_2}{\partial x_i} + \frac{2}{3} \frac{\partial u_k}{\partial \xi_2} \frac{\partial \xi_2}{\partial x_k} \delta_{ij} \right]_w \quad (1)$$

where  $u_i$  represent the components of the velocity in the Cartesian reference system, and  $\mu$  is the molecular viscosity. The equation (1) requires the evaluation of velocity derivatives in the wall-normal direction, and of the metric coefficients.

The wall functions approach allows to compute the velocity derivatives by employing the expression of the wall shear stress

$$\tau_{wi} = \mu \left( \frac{\partial u_i}{\partial \xi_2} \right)_{\xi_2=0} \quad (2)$$

that can be evaluated through the friction velocity  $u_\tau$ .

The friction velocity is related to the components of the tangential velocity vector  $u_{t,i}$  by the following relation, that holds in the logarithmic region of a boundary layer :

$$u_{\tau,i} = \frac{u_{t,i}}{\frac{1}{\kappa_a} \log(\xi_2^+) + B} \quad (3)$$

where  $\xi_2^+ = \xi_2 u_\tau / \nu$  is the distance in wall coordinates,  $\kappa_a \cong 0.4$  is the Kármán constant,  $B \cong 5$ ,  $\rho$  is the density, and  $\nu = \mu / \rho$ .

The singularity of equation (3) at separation or re-attachment points (where  $u_\tau \rightarrow 0$ ) is removed by computing the velocity scale from the expression of the turbulent kinetic energy in the logarithmic layer:

$$\kappa = \frac{u^2}{\sqrt{\beta^*}} \quad (4)$$

with  $\beta^* = 0.09$ . As a consequence in equation (3) the distance  $\xi_2^+$  is replaced by  $\xi_2^* = \frac{\xi_2 u^*}{\nu}$  with  $u^* = \beta^{*0.25} \sqrt{\kappa}$ .

The classical wall functions formulations require the first computational point be located in the log layer. This issue can be addressed by considering the intersection  $\tilde{\xi}_2$  between the viscous and the log region of a boundary layer [1]. This point can be computed by equating the linear and logarithmic laws of the velocity :

$$\xi_2^+ = \frac{1}{\kappa_a} \log(\xi_2^+) + B \Rightarrow \tilde{\xi}_2 \cong 11 \quad (5)$$

and equation (4) is changed to

$$u_{\tau,i} = \frac{u_{t,i}}{\frac{1}{\kappa_a} \log(\tilde{\xi}_2^*) + B} \quad (6)$$

with  $\tilde{\xi}_2^* = \max[\xi_2^*, \tilde{\xi}_2]$ .

The components of the tangent velocity vector are still needed to calculate the friction velocity. The  $u_{t,i}$  can be evaluated, by considering that

$$u_t = u - (u \cdot n)n \quad (7)$$

where  $n$  is the unit vector normal to the wall.

The friction velocity is computed iteratively by equation (6), and the components of the wall shear stress are evaluated as

$$\tau_{wi} = -\rho u_{\tau,i} \max[u_{\tau,i}, u^*] \quad (8)$$

The velocity derivatives needed for equation (1), are obtained by comparing equation (8) with equation (2).

The metric coefficients  $\frac{\partial \xi_2}{\partial x_i}$  are computed by considering the components of the normal area vector  $S_i$  of the face of a computational cell as :

$$\left. \frac{\partial \xi_2}{\partial x_i} \right|_w = \frac{S_i}{S} \quad (9)$$

with  $S = \sqrt{S_1^2 + S_2^2 + S_3^2}$  the area of the cell face.

### Turbulence Equations

The  $\kappa$ - $\omega$  turbulence model is considered. The followed approach consists in resolving the transport equation of the turbulent kinetic energy and imposing the turbulent specific dissipation rate in the first cell by employing the analytical solution of  $\omega$  in the viscous and log layer [3]. The  $\kappa$  equation is integrated by imposing

$$\left. \frac{\partial \kappa}{\partial \xi_2} \right|_w = 0 \quad (10)$$

as wall boundary condition. The production of  $\kappa$  reads as

$$P_\kappa = \tau_{ij} \frac{\partial u_i}{\partial x_j} \quad (11)$$

and involves the velocity derivatives. In the first computational cell, it is possible to write:

$$P_\kappa = \tau_{11} \frac{\partial u_1}{\partial \xi_2} \frac{S_1}{S} + \tau_{22} \frac{\partial u_2}{\partial \xi_2} \frac{S_2}{S} + \tau_{33} \frac{\partial u_3}{\partial \xi_2} \frac{S_3}{S} + \tau_{12} \left( \frac{\partial u_1}{\partial \xi_2} \frac{S_2}{S} + \frac{\partial u_2}{\partial \xi_2} \frac{S_1}{S} \right) + \tau_{13} \left( \frac{\partial u_1}{\partial \xi_2} \frac{S_3}{S} + \frac{\partial u_3}{\partial \xi_2} \frac{S_1}{S} \right) + \tau_{23} \left( \frac{\partial u_2}{\partial \xi_2} \frac{S_3}{S} + \frac{\partial u_3}{\partial \xi_2} \frac{S_2}{S} \right) \quad (12)$$

where equation (9) has been applied. The velocity derivatives in equation (12) are evaluated by the approach described in the previous section.

The transport equation of the turbulent specific dissipation  $\omega$  is not solved in the first cell close to a solid boundary. The value of  $\omega$  is imposed as

$$\omega = \sqrt{\omega_v^2 + \omega_l^2} \quad (13)$$

by considering the solution of the viscous layer

$$\omega_v = \frac{6\mu}{\rho \beta \xi_2^2} \quad \text{with } \beta = 0.075 \quad (14)$$

and of the logarithmic layer

$$\omega_l = \frac{u_\tau}{\sqrt{\beta^* \kappa_a \xi_2}} \quad (15)$$

In equation (15),  $u_\tau$  is replaced by  $u_\omega = \max[u_\tau, u^*]$ .

### Numerical Method

The wall function formulation has been implemented in the CIRA flow solver ZEN (Zonal Euler Navier -Stokes). ZEN is a multi-block very robust, efficient and well assessed solver for the Euler and RANS equations based on a finite-volume cell-centred approach. A central differencing scheme with blended self adaptive second and fourth order artificial dissipation is employed. The solution procedure is based on a pseudo time-marching concept. The multi-grid scheme is used to accelerate the convergence of the solution by using the Runge-Kutta algorithm with local time stepping and residual averaging, on different grid levels. Several turbulence models, ranging from algebraic to high order models, are implemented and have been tested on several practical applications [4]. The  $\kappa$ - $\omega$  model proposed by Kok [5], [6] has been applied for the simulations presented in this paper. A time-accurate version

of the solver has been developed and is currently under validation.

**Results and discussion**

The method has been applied to simulate the transonic flow around the RAE 2822 airfoil, and the subsonic flow in high lift conditions around a three-component airfoil and a wing-body configuration.

*RAE 2822 airfoil*

The transonic flow around the RAE 2822 airfoil presents a strong shock-boundary layer interaction with an induced separation. The flow conditions, named in literature [7] as case 9 and case 10 have been considered.

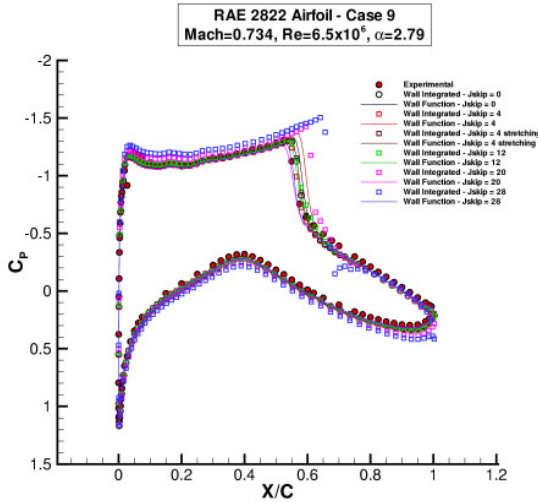


Fig. 1

Several computational grids have been generated. The finest mesh has 273x81 points, while the other grids have been obtained by removing the first (4, 12, 20, and 28) grid lines in the wall-normal direction. An other mesh has been obtained by skipping 4 points and trying to keep the same stretching ratio as the original mesh. The finest grid presents values of  $y^+$  for the first layer of cells even less than 1, and the coarsest greater than 140.

The pressure coefficient is presented in the figures 1 and 2 for cases 9 and 10 respec-

tively. Experimental data [7] are also shown as a reference. The wall functions work in a satisfactory way on all the meshes considered.

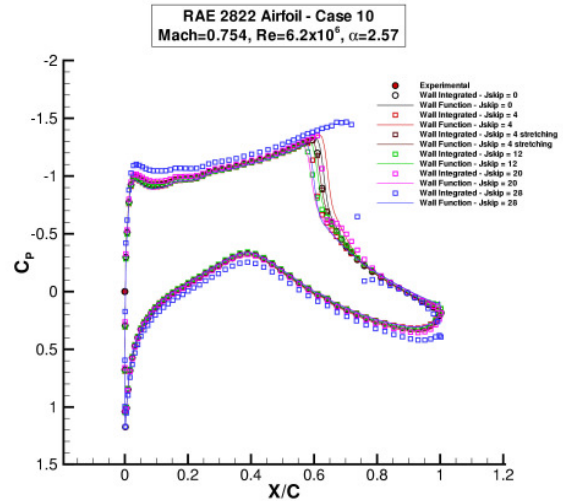


Fig. 2

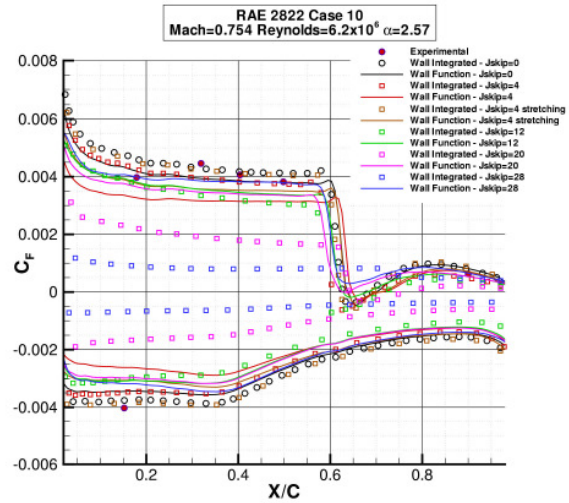


Fig. 3

The wall integrated results are not acceptable on the two coarsest grids (jskip=20, and 28). A weak dependence of the shock location on the  $y^+$  of the first layer of cells is shown. The results achieved on the finest and on the grid generated taking care of the stretching ratio are the closest to the wall-integrated data. The friction coefficient for the case 10 is reported in fig. 3. Flow separation occurs downstream the shock on all the grids except on those generated by removing 20 and 28 points. Results achieved on the two coarsest grids by

applying standard wall boundary conditions are clearly unacceptable. All the simulations have been performed by assuming fully turbulent conditions.

### A310 Wing Section

The formulation has been applied to simulate the high lift flow around a three-component airfoil in landing configuration. The geometry chosen is the 59% wing span section of the A310 aircraft. For this case experimental data at Mach number of about 0.22, and Reynolds number of about 4 million are available.

Table 1

Grid Number	Points	$y^+$ at $\alpha = 12^\circ$		
		Slat	Main	Flap
1	159160	12	7	5
2	159160	70	50	35
3	159160	80	60	50
4	159160	100	70	60
5	145448	90	50	40

The wall function formulation has been tested at  $\alpha = 12^\circ$  on several grids. Starting from the finest mesh (N. 1), the others (N. 2,3, and 4) have been generated by increasing the thickness of the first layer of cells and keeping the same number of points. The last mesh (N. 5) has been obtained with  $y^+$  of the same order of magnitude as grids 2, 3, and 4, and decreasing the number of points. The  $y^+$  of the first layer of cells (at  $\alpha = 12^\circ$ ) in the expansion region of each component, and the number of points are reported in table 1.

The plots of the pressure coefficient computed at  $\alpha = 12^\circ$  by wall integrating and applying the wall function formulation are reported in fig. 4. The wall functions on grid 1 and 2 reproduce the wall integrated results obtained on the finest mesh. On the grids 2, 3,

and 4 an over-estimation of the  $C_p$  in the upper side of the components is visible in the results achieved by standard wall boundary conditions. An under-estimation of the pressure coefficient is present in the results obtained by the wall functions on grids 3, 4, and 5. This behaviour is more consistent with the fully turbulent assumption.

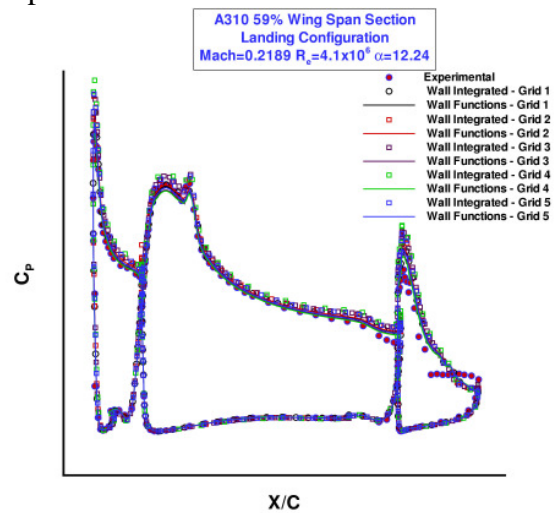


Fig. 4

Differences are present also on the flap. Wall functions, as the wall-integrated simulation on the finest grid, provide an attached flow. A separation instead is obtained at the trailing edge zone of the flap when standard boundary conditions are applied on grid 2, 3, 4, and 5.

Experimental data are also shown in fig. 4. The agreement with the numerical results is very good. The discrepancy between numerical and experimental results on the flap (large flow separation) is present in many other numerical simulations [4], [8].

Grids 1 and 5 have been used to perform computations at several incidences. The pressure coefficient achieved at  $\alpha = 22^\circ$ , just before the stall, is shown in fig. 5. Results achieved by applying the wall functions on grid 5 are practically coincident with the wall integrated pressure coefficient obtained on the mesh 1. An under-prediction of the pressure coefficient on the upper side of both the main

component and flap is visible. This is partly due to the fact that fully turbulent conditions have been assumed. In fact, the comparison with experimental data has been improved by imposing the transition points. The numerical results become closer to the experiments over the complete upper surface of the main component and flap.

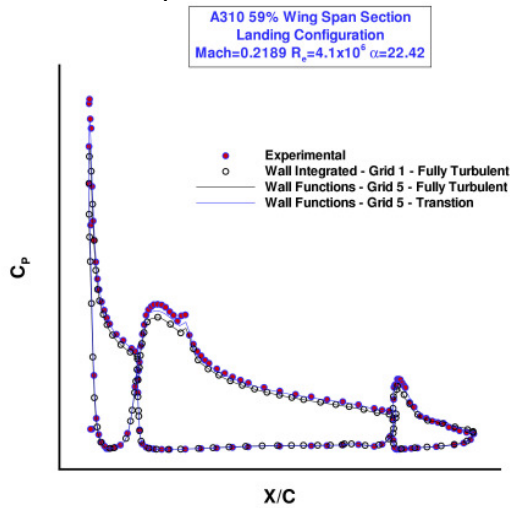


Fig. 5

The lift and drag coefficients are presented in the figures 6 and 7 respectively. The complete polar of the airfoil has been computed by applying the wall functions on mesh 5. Simulations at a couple of incidences have been performed by using standard wall boundary conditions on grids 1 and 5 and the proposed approach on mesh 1. Experimental data are also shown as a reference.

The wall functions reproduce on grid 5 both the lift and drag coefficients obtained on the finest grid 1 by wall integrating the NS equations. An appreciable difference in the results on grid 1 and 5 achieved by standard boundary conditions is visible. On the contrary wall functions provide results that do not depend too much on the  $y^+$  of the wall-adjacent layer of cells. The difference between fully turbulent conditions and considering a flow that undergoes a transition is evident. In particular almost the same  $C_l$  measured in the experiments is obtained when the

wall functions have been applied on grid 5 with imposed transition points.

The wall integrated drag coefficients achieved on grid 5 are closer to the experimental data than results achieved on the finest grid 1. However this is not very relevant to the verification of the approach presented. The main goal of applying the wall functions is the simulation of very high Reynolds number flows at a reasonable computational cost. The formulation has been tested by reproducing on a coarse mesh the results than can be obtained on a finer mesh with lower values of  $y^+$ .

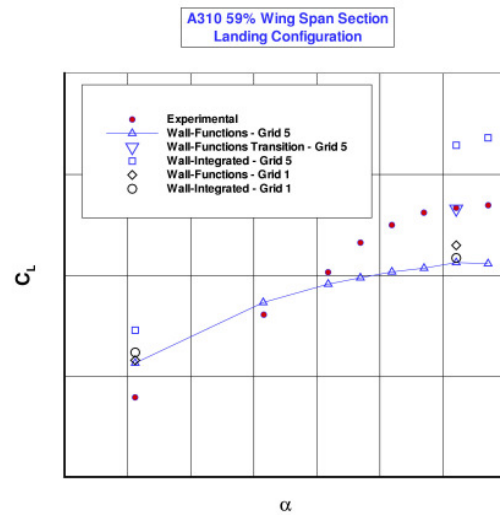


Fig. 6

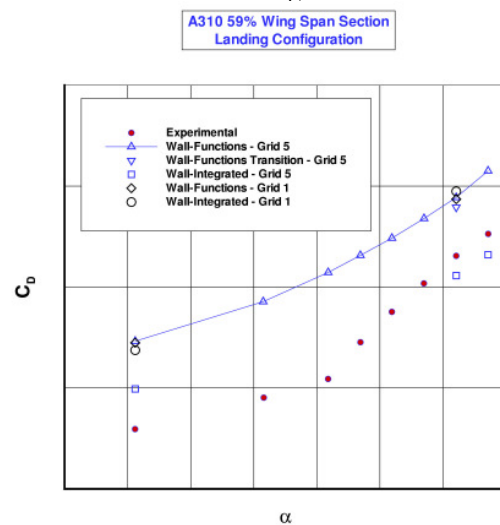


Fig. 7

*KH3Y Wing-body Configuration*

The KH3Y configuration is a wing-body equipped with full-span slat and flap tested at low Reynolds number in the AIRBUS-D tunnel and at high Reynolds number in the ETW tunnel. Simulations were performed at Reynolds number  $1.3 \times 10^6$  employing a structured multi-block grid of about 2 million points. The same mesh is used to compute the flow at Reynolds number  $1.5 \times 10^7$  applying the wall function approach. Fully turbulent flow conditions have been assumed.

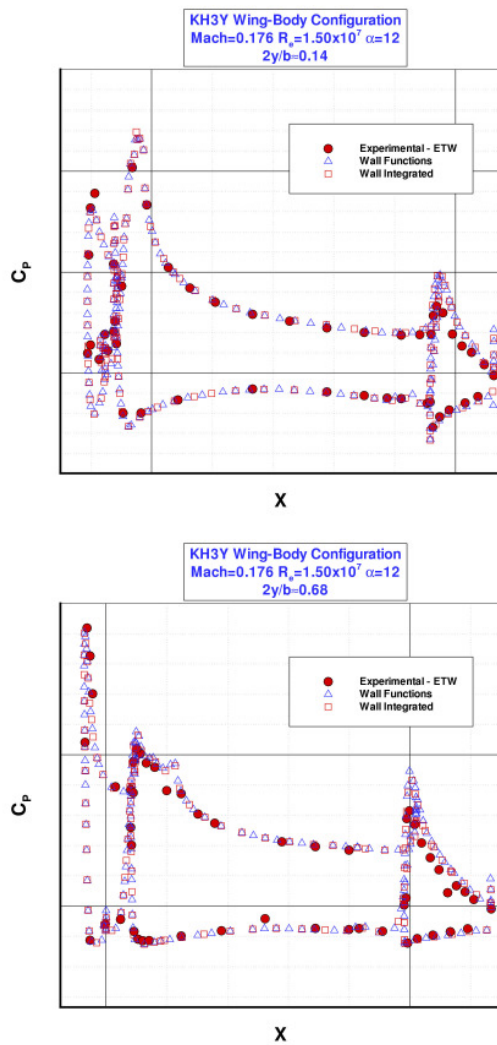


Fig. 8

Despite the large Reynolds number, the values of  $y^+$  are not particularly critical. The highest values are obtained in the leading

edge region of the root sections and are of order of magnitude 10. Several incidences have been considered. Only the results, in term of pressure coefficient, achieved at  $\alpha = 12^\circ$  in the linear range of the lift curve, and at  $\alpha = 18.5^\circ$  close to the stall, are discussed here. The  $C_p$  at  $\alpha = 12^\circ$  is presented in fig. 8. The results achieved by applying the wall functions and standard boundary conditions are practically coincident, as could be expected by considering the values of  $y^+$ .

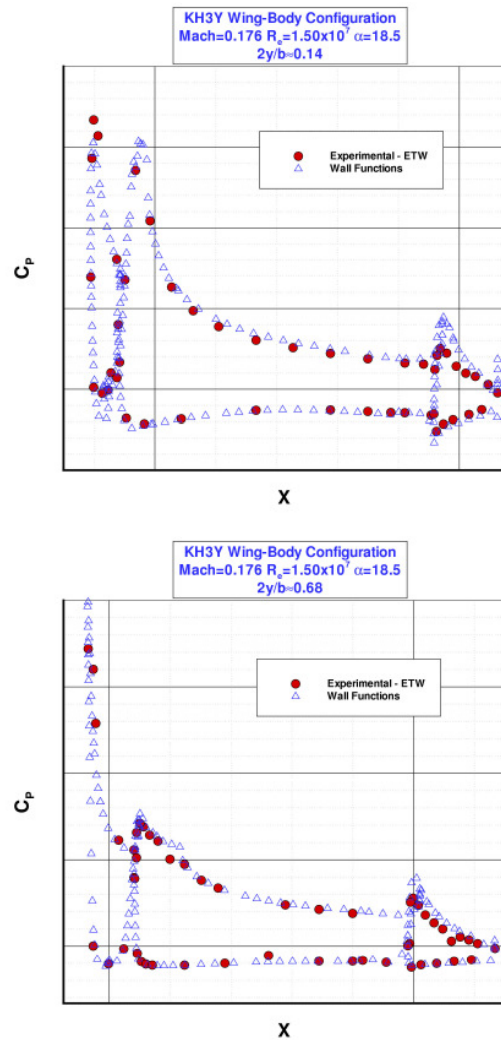


Fig. 9

A good comparison with the experimental data is obtained. An over-estimation of the pressure coefficient on the upper surface of the

flap is present and becomes more pronounced at the outboard sections of the wing.

At  $\alpha = 18.5^\circ$  (fig. 9) wall-integrated results are not shown because it has not been possible to reach a good convergence level. The wall functions instead have allowed to obtain a solution that compares quite well with experimental data. The discrepancy on the flap is present also at this incidence. It is worth pointing out that a similar behaviour, in terms of pressure coefficients, has been shown by other wall integrated numerical simulations performed during the EUROLIFT I project on a grid properly generated for the Reynolds number  $1.5 \times 10^7$ . The effect of imposing transition points should be assessed.

### Conclusion

A scalable wall function approach has been presented. The formulation has been tested for a transonic flow with a shock-induced separation, and for the high lift flow around a three component airfoil and a wing body configuration. The 2D cases have been investigated by generating grids with large values of  $y^+$ . The 3D simulations have been performed by employing a mesh generated for a lower Reynolds number case. The wall functions have enhanced the robustness of the numerical method, always providing reasonable results. A weak dependence of the shock location on  $y^+$  has been noted. Flow separation has been correctly predicted for both the transonic and high lift flows considered. The results achieved by wall integrating the NS equations on fine grids have been reproduced by applying the wall functions on coarser grids with larger values of  $y^+$ . The final goal is the simulation of flows at flight Reynolds number. The formulation has been applied to

a  $\kappa\text{-}\omega$  turbulence model, and will be extended to  $\kappa\text{-}\epsilon$  and Spalart-Allmaras models.

### Acknowledgements

The work and the results presented in this paper have been performed within the European project EUROLIFT II, under contract no. AST2-2004-502896, being sponsored by the European Commission in the 6<sup>th</sup> framework programme. The authors are particularly grateful to Dr. Ralf Rudnik from DLR, Dr. Juergen Quest from ETW, and Dr. Peter Eliasson from FOI to have kindly provided the experimental data for the KH3Y wing-body configuration.

### References

- [1] Grotjans H, Menter F. Wall functions for general application CFD codes. *Proc. 4<sup>th</sup> European Computational Fluid Dynamics Conference*, Athens, John Wiley & Sons Ltd., pp. 1112-1117, 1998
- [2] Thiede P. EUROLIFT – Advanced high lift aerodynamics for transport aircraft. *Air & Space Europe*, Vol. 3, No. 3/4, pp. 1-4, 2001
- [3] Wilcox D.C. Turbulence modelling for CFD. 2nd edition, DCW Industries, Inc., 1994
- [4] Catalano P, Amato M. An evaluation of RANS turbulence modelling for aerodynamic applications. *Aerospace Science and Technology Journal*, Vol. 7, No. 7, pp. 493-509, 2003
- [5] Kok J. Resolving the dependence on free-stream values for the  $\kappa\text{-}\omega$  turbulence model. *AIAA Journal*, Vol. 38, No. 7, pp. 1292-1295, 2000
- [6] Catalano P, Amato M. Assessment of  $\kappa\text{-}\omega$  turbulence modelling in the CIRA flow solver ZEN. *ECCOMAS 2001 CFD Conference*, September 4<sup>th</sup>-7<sup>th</sup> 2001, Swansea, Wales (UK)
- [7] AGARD-AR-138. Experimental data base for computer program assessment.
- [8] Eliasson P. CFD improvements for high lift flows in the European project Eurolift. *AIAA paper 2003-3795, 21<sup>st</sup> Applied Aerodynamics Conference*, June 23<sup>rd</sup>-26<sup>th</sup> 2003, Orlando (FL)